Additive manufacturing of WC reinforced maraging steel 300 composites by cold spraying and selective laser melting

Xingchen Yan, Chunjie Huang, Chaoyue Chen, Rodolphe Bolot, Lucas Dembinski, Renzhong Huang, Wenyou Ma, Hanlin Liao, Min Liu

Additive manufacturing of WC reinforced maraging steel 300 composites by cold spraying and selective laser melting

Xingchen Yan[1, 2], Chunjie Huang[1]*, Chaoyue Chen[1]*, Rodolphe Bolot[1], Lucas Dembinski[1], Renzhong Huang[2], Wenyou Ma[2], Hanlin Liao[1], Min Liu[2]

1. *LERMPS, ICB UMR 6303, CNRS, Univ. Bourgogne Franche-Comté, UTBM, F-90010 Belfort, France*

2. *National Engineering Laboratory for Modern Materials Surface Engineering Technology; The Key Lab of Guangdong for Modern Surface Engineering Technology; Guangdong Institute of New Materials, Guangzhou 510651, P.R. China*

Abstract: Till now, additive manufacturing (AM) technologies based on different principles have been widely applied to produce metal matrix composites (MMCs). In this study, AM technologies of cold spraying additive manufacturing (CSAM) and selective laser melting (SLM) were used to manufacture maraging steel 300 (MS300) composite reinforced by WC particles. The results show that the SLM composite possesses a relatively higher densification rate and a lower porosity than that of the CSAM composite. Dry sliding wear test and microhardness measurements were performed to characterize the mechanical properties. The CSAM composite possesses a slightly higher microhardness value than that of the SLM composite. However, the SLM composite shows a significantly lower wear rate than that of the CSAM composite, presenting a stable evolution of the friction coefficient and a worn morphology without obvious scratches. However, these differences in the mechanical properties can be contributed to the distinct evolution features of the WC reinforcement particle during these two AM processes. Through understanding the composite formation mechanisms and the WC evolution, it is possible to provide a guidance for application of the different AM technologies for preparation of MMCs.

Keywords: Cold spraying; selective laser melting; WC; maraging steel 300; microstructure; tribological behavior

*Corresponding author: Chaoyue CHEN, email: chaoyue1987@gmail.com, Chunjie HUANG, email: chunjie.huang@utbm.fr

1. Introduction

At the opposite of traditional subtractive manufacturing technologies, metal additive manufacturing (AM) enables the production of parts directly from a 3D data [1, 2]. Owing to their unique advantages in avoiding material waste and design complexity, AM methods have drawn many attentions. In AM approaches, the part is built up by consecutive fabrication of layers, which enables the production of components with high complexity [3, 4]. Nowadays, several types of AM technologies have been developed based on approaches such as fusion of a powder bed thanks to a high-energy input [5] or particle deposition in solid state [6, 7]. Due to the distinct underlying theories and technical characteristics, different resulting material properties and microstructures can be provided by these different approaches.

Generally, AM technologies via powder bed fusion (PBF) include processes like selective laser sintering (SLS) [8], selective laser melting (SLM) [9], direct metal laser sintering (DMLS) [10], direct metal laser melting (DMLM) [11], and electron beam melting (EBM) [5]. Currently, AM approaches based on the fusion of a metal powder bed tend to use melting rather than sintering to build components with high density. As an additive manufacturing technology, selective laser melting (SLM) allows the production of complex parts by the fusion and consolidation of successive powder layers by a laser beam, according to a pattern conceived by computer aided design (CAD). The rapid solidification of the molten pool after fusion, and the thin weld of each layer can provide a high density material with high mechanical properties.

On the contrary, the cold spray (CS) technique [12, 13] aims at fabricating the sample through the solid-state deposition of powders. In this process, the spray particles are accelerated to a very high velocity by a supersonic gas flow. The successful bonding of particles occurs through the intensive plastic deformation upon high-velocity impact in a solid-state at a temperature below the melting point of the sprayed materials [14-16]. This intensive plastic deformation can break the thin oxide film on the surface of the substrate or previously deposited particles, and promote the intimate contact between the fresh metal surface, which can lead to a strong metallurgical bonding. Consequently, the problems inherent to high temperature and metling deposition processes, such as serious oxidation, phase transformations and thermal stresses, can be minimized or eliminated in the cold sprayed components [17, 18]. The unique cold feature (i.e., below the melting point) of the CSAM process enables the production of components from temperature sensitive material [19, 20] such as nanocrystalline and

amorphous materials as well as oxygen-sensitive materials like aluminum [21, 22], copper [13], and titanium [23-25]. Thus, cold-spray additive-manufacturing (CSAM) has been recognized as a useful and powerful process for additive manufacturing. As reported by Pattison et al [6], the cold spray additive manufacturing with various building strategies and material selections can be considered as a novel freeform fabrication technique for functional components. Dupuis et al [26] fabricated pin fin arrays by using the cold spray additive manufacturing process and characterized its thermal and hydraulic performance. Moreover, with its inherent advantages like no phase change, large fabrication size, low oxidation and high fabrication rate, cold spray additive manufacturing was also applied as an method to repair dimensional defects [21, 27].

Currently, the application of AM technology is mainly focused on the manufacturing of functional metallic parts [28], including metals, alloys and metal matrix composites (MMCs). Recently, many MMCs, e.g., TiC reinforced Fe alloys [29, 30], SiC and Al2O3 reinfroced Al alloys [31-33], TiC reinforced Ti alloys [34-37], have been successfully prepared by SLM. Maraging steel 300 (MS300) is an iron–nickel alloy with absence of carbon, which uses elements such as molybdenum, cobalt, titanium and aluminium as substitutes to produce precipitation-hardening in iron-nickel martensitic [38, 39]. Other than its outstanding properties suach as good mechanical strength, toughness, weldability and resistance to crack propagation, more recent interests have been paid on the high tribological performances of MS, which can extend its applications [40]. However, the fabrication of MS300 has not been reported by the technique of cold spray additive manufacturing.

Therefore, considering the aforementioned respective merits of different AM technologies, the CSAM and SLM processes were proposed in this work to fabricate MS300 composites reinforced by WC particle (WC/MS300). Due to its favorable wettability with iron alloy particles, WC was proposed as reinforcement, to improve the wear resistance of iron-based composite materials. The present work mainly focused on the description of the microstructure and tribological behavior of WC/MS300 composites manufactured by CSAM and SLM processes. Through the comparison between the samples prepared by CSAM and SLM, the corresponding characteristics of different AM technologies are discussed.

2. Materials and experimental procedures

2.1. Materials

A blending mixture (see Fig. 1a) of spherically gas atomized MS300 powder (EOS GmbH, Germany) with a size range of 33-40 μm and an irregular WC powder (XIAMENJINGLU, China) with a size range of 1-6 μm was used as starting materials. Based on the literature study, the size distribution of reinforcement WC particle can be benefical for the high deposition efficiency in CS [41] as well as powder paving in SLM [42]. The MS300 feedstock power has a microhardness value of 363.3±55 $Hv_{0.2}$. These two powders with a weight ratio of 85/15 were mechanically blended in a tumbling mixer during 200 min before fabrication.The cross-sectional morphology of the etched MS300 powder is shown in Fig. 2a and the detailed grain structure in Fig. 2b. The chemical composition of MS300 is given in Table. 1.

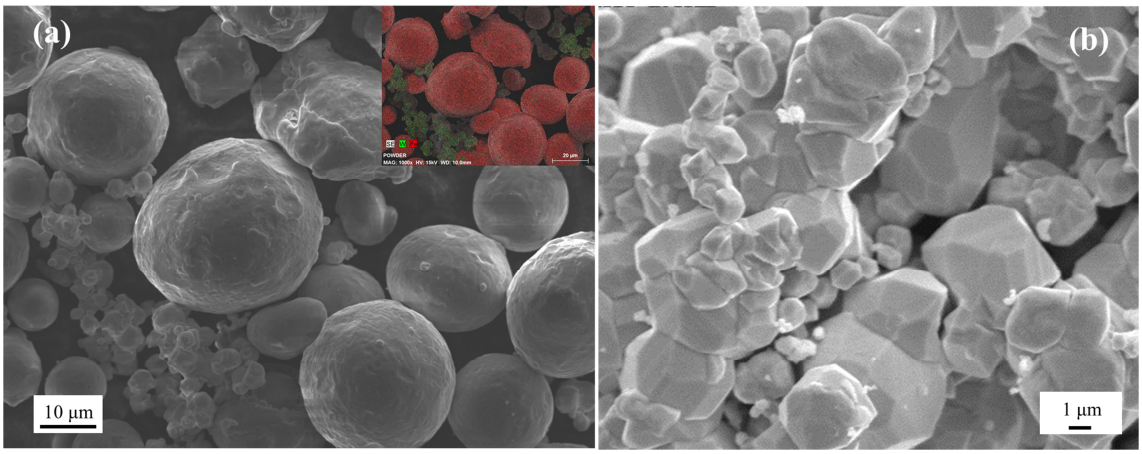

Fig. 1 SEM morphologies: (a) blending mixture of feedstock powders with the EDS mapping show each item (MS300 in red and WC in green), (b) WC.

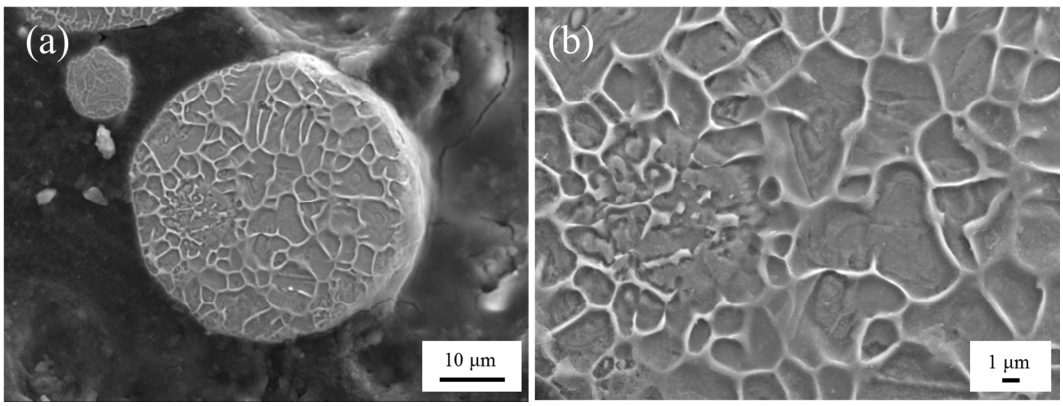

Fig. 2 Cross-section showing the grain structure of a MS300 particle after etching: (a) overview, (b) in detail.

Table 1. Chemical compostion of MS300 powder.

Element	Fe	Ni	Co	Mo	Ti	Al	Cr,Cu	C	Mn, Si	P, S
wt%	balance	17-19	8.5-9.5	4.5-5.2	0.6-0.8	0.05-0.15	≤0.5	≤0.03	≤0.1	≤0.01

2.2. Experimental procedures

The WC/MS300 composite was firstly fabricated with a PCS-1000 cold spray system (PLASMA, Japan). Nitrogen was used as carrier gas whereas air with a pressure of 3.0 MPa and a temperature of 500 ^{o}C was used as propelling gas. The standoff distance from the nozzle exit to the substrate surface was 30 mm. The hatch distance between successive pathes was 2 mm. The nozzle was kept perpendicular to the substrate for a maximum deposition efficiency. In addition, the nozzle traverse speed was 100 mm/s. A grit-blasted 304 stainless steel plate (40 mm × 50 mm) was used as substrate.

Another WC/MS300 composite was produced by an EOS M290 system (EOS GmbH, Germany) equipped with an Yb-Fiber laser (1064 nm) with a maximum power of 400 W. The diameter of the laser beam focus spot (100 μm), laser power (285 W), layer thickness (50 μm), hatch distance (50 μm) and moving speed of the laser beam (960 mm/s) were kept constant during manufacturing. The fabrication by SLM was operated in a chamber filled by nitrogen with a residual volumetric oxygen content lower than 1.3 % to avoid oxidation. Cubic SLM specimens with dimensions of 15 mm × 15 mm × 8 mm were prepared.

The polished composites were etched at room temperature for 20 s with a solution of 25 ml HNO_3, 50 ml HCl, 1 g $CuCl_2$ and 100 ml distilled water. The microstructure was then observed by scanning electron microscopy (SEM), with a device equipped with an energy-dispersive spectroscopy (EDS) unit

(JSM5800LV, JEOL, Japan). Phase identification was performed by X-ray diffraction (XRD, Siemens, Germany) using a Cobalt anticathode (k = 1.78897 Å) operated at 35 kV and 40 mA. The cross-section density of the samples was calculated by image analysis (NIH Image J, Software, USA) based on optical microscopy (OM) images, and 15 measurements were carried out for each sample. The Vickers hardness was measured using a microhardness tester (Leiz-Wetzlar, Germany) at a load of 200 g and an indentation time of 25 s. Vickers hardness measurements were carried out at different locations on the cross-section, and the indicated values are the average of 15 measurements. The wear cross-sections of the worn composites was measured with a Profilemeter (AltiSurf 500, Altimet, France). Besides, scanning transmission electron microscopy (STEM) observations and energy-dispersive X-ray spectroscopy (EDX) mappings were carried out on the JEOL 2100F transmission electron microscopy (TEM) operating at 200 kV. The sample was prepared by focused ion beam (FIB, Nanolan-450S, FEI) with Ga liquid metal ion source.

Dry sliding wear tests were conducted at ambient temperature with a CSEM tribometer implement (Switzerland). Before the tests, the roughness *Ra* of the sample was kept less than 0.15 μm to rule out its influence wear performance. The counterpart material was a WC/CO ball with 6 mm diameter, which was grinded and polished using sandpaper and cleaned with ethanol before the tests. The friction test load was 500 g, with a rotational speed corresponding to 100 mm/s for 100 m with the radius of 3 mm. The coefficient of friction (COF) was recorded during sliding. After friction test, the surface of worn samples was observed by SEM and then analysed by EDS. The cross-sections of the worn tracks were measured by an Altisurf 500 profilometer (France). The worn volumes of the samples were calculated via the product of the cross-sectional areas by the length of worn tracks.

3. Results and discussion

3.1. Phase analysis

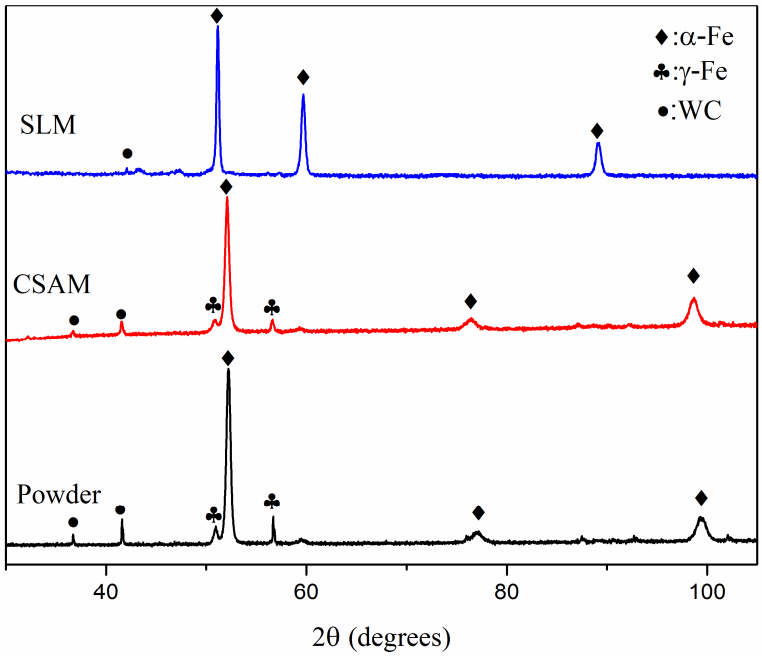

Fig. 3 XRD analysis of the starting powder, the CSAM composite and the SLM composite.

Fig 3. shows the XRD patterns of the starting powder, the CSAMed and the SLMed composite parts. At a wide range of 2θ between 30° and 105°, it can be noticed the strong diffraction peaks indexed to α-Fe and γ-Fe that belong to maraging steel 300. Meanwhile, weak peaks of WC reinforcing phase were also observed. The comparison of XRD spectra of the starting powder and the CSAM composite indicates that no melting and phase transformation occurred during the fabrication of the cold sprayed WC/MS300 composite, because no other phase was detected. This fact clearly demonstrates the unique 'cold' feature of the cold spray process in preventing melting and phase transformations.

As for the XRD pattern of the SLM composite, the main phase is obviously martensitic. Such martensitic phase was formed during the rapid solidification occurring during the SLM process. Besides, the diffraction peaks of WC are almost eliminated by the SLM process, implying the refinement and vanishing of the reinforcement particles. Such phenomenon is due to the melting of

both powders and forthcoming reaction between the molten metals and WC particles under the high-energy input by the laser beam.

3.2. Microstructure and porosity

The etched cross-section morphologies of WC/MS300 composites fabricated by CSAM and SLM are presented in Fig. 4. As shown in Fig. 4a (CSAM process), the MS300 particles are found to experience a severe deformation, acting as the matrix, whereas hard WC particles acting as the reinforcement phase are embedded in the matrix. It can be noticed that a severe plastic deformation of MS300 particles led to obvious grain elongation, while no trace of deformation is observed for the WC phase. During deposition, MS300 particles were deformed through both the impact of successive MS300 particles and the relatively hard and heavy WC particles. Such different particle deformation features resulted in the intimate contact interface between the metal matrix and WC particles. In Fig. 4b, dendritic solidification patterns distributed on the cross-section and perpendicular to the layer addition direction can be found. Each molten shape is clearly visible and welded together without obvious flaws. Compared with the cold sprayed sample (Fig. 4a), less WC phase was found in the SLM one. Due to the high thermal energy input input by the laser beam during SLM, the WC particles experienced partial melting in the molten pool.

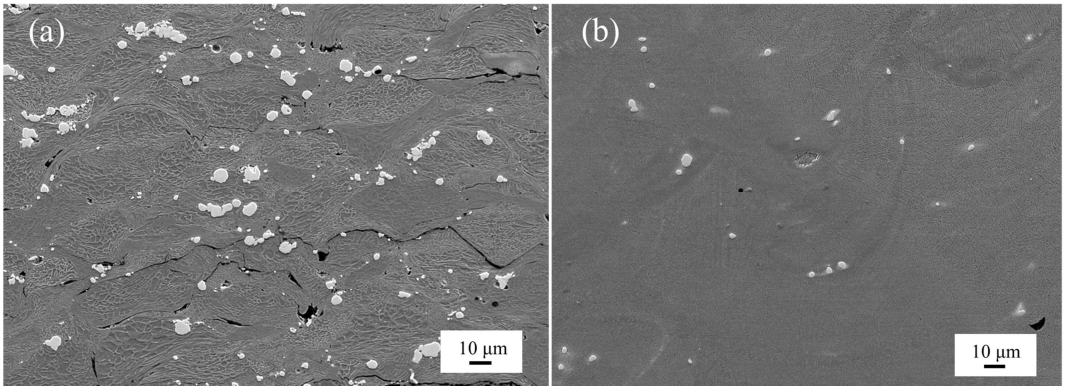

Fig. 4 SEM micrographs of composites fabricated via CSAM (a) and SLM (b) processes.

Furthermore, different porosity levels and relative density can be observed for the composites prepared by the two methods. As shown in Fig. 4, obvious pores and cracks can be seen in the CSAM composite, while the microstructure of SLM composite is more homogeneous with less pores. In order to quantitify the comparison, the relative densification rates of both composites were measured and given in Fig. 5. As shown in Fig. 5, the SLM composite with a relative density of 99.6% possesses a relatively denser morphology than that of CSAM composite with a density of 98.3%. Due to the lower

melting temperature in comparison with the WC phase, the MS300 phase was completely liquefied under the effect of the high thermal energy input by the laser beam. The favorable wettability of WC particles with the MS300 matrix is also advantageous to form a dense specimen. However, as shown for the case of the CSAM sample in Fig. 4a, the relatively hard WC particles lacked sufficient plastic deformation. Owing to the strong covalent bonding, WC cannot easily experience severe plastic deformation. Thus, most WC particles will penetrate into the relatively soft MS300 matrix rather than plastic deformation. Such incomplete compaction effect [43] results in a higher porosity of 1.7% than that of SLMed composite with a prorosity level of 0.4%.

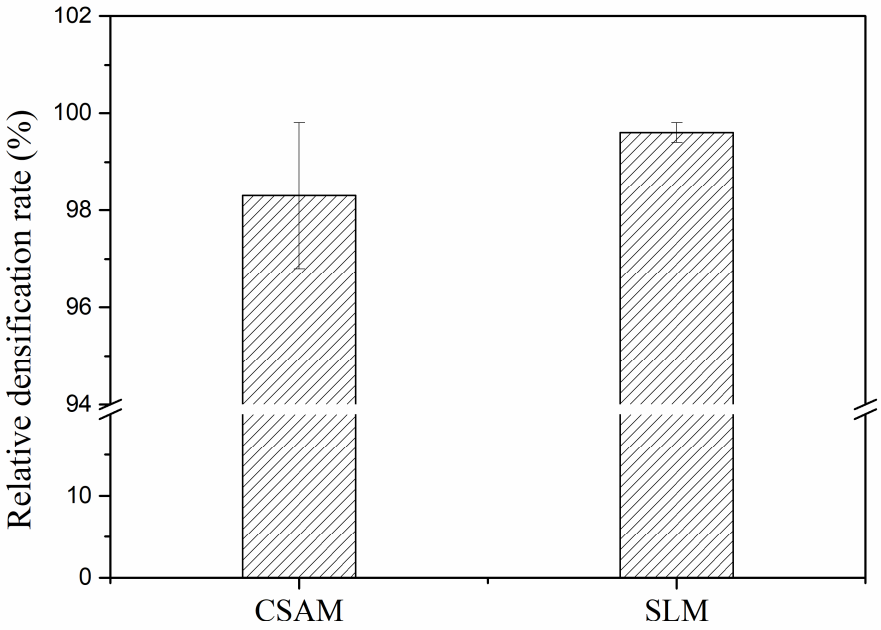

Fig. 5 Relative densification rate of the two composites manufactured by CSAM and SLM.

3.3. Microhardness

Fig. 6 shows the microhardness values of WC/MS300 composites manufactured by CSAM and SLM. It can be seen that the CSAM-processed sample possesses a hardness of 394 $HV_{0.2}$, whereas the average hardness of the SLM-processed sample is about 385 $HV_{0.2}$. It should be noted that in order to obtain relatively accurate microhardness values, the indenter was located so as to avoid the hard WC phase. However, it is unavoidable to contact WC particles for the CSAM sample which contains more remaining WC than the SLM part. In a way, it helps to improve the test value of the microhardness of

the CSAM-processed sample. It should be noticed that compared with original feedstock (363 $HV_{0.2}$), the microhardness of composites were slightly improved after both SLM and CSAM process. The microhardness of starting MS300 particles is 286 $HV_{0.2}$. Compared with the starting material, the improvement of microhardness was considered to be caused by the reinforcement by WC particles. New hard metal compounds can be composed by releasing C and W elements from partial molten WC particles into the molten pool of the metal matrix, whichi is discussed in detailed through STEM observation. As shown in Fig. 4b, the WC particles are uniformly distributed in the denser MS300 matrix, which contributes to the microhardness improvememt. It can be concluded that WC particles play a major role in the increase of the microhardness of the composite samples. Owing to the rapid melting and solidification characteristic of the SLM process, the SLM composite shows a finer microstructure compared with that of the CSAMed sample, which can also contribute to improve the microhardness.

However, the CSAM composite possesses a relatively higher microhardness than that of the SLM composite. Due to the different formation mechanisms of the composite, a different strengthening mechanism exists in the CSAM composite. Such phenomena can be considered to be promoted by the strain or work hardening of a cold sprayed structure. As shown in Fig. 4a, due to the plastic deformation under the successive impact of high-velocity particles and the tamping effect caused by hard WC particles, the MS300 particles undergo a severe work-hardening, which leads to the increase of CSAM composite microhardness [44]. In addition, the uniformly dispersed WC particles also contribute to the increase of the overall hardness by restricting the deformation of the soft MS300 matrix.

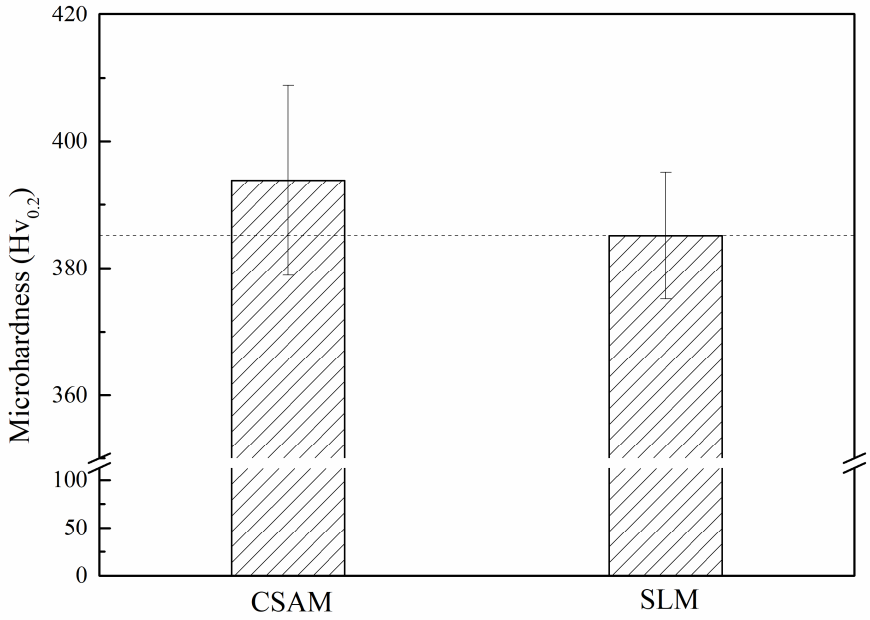

Fig. 6 Microhardness of composites manufactured by CSAM and SLM.

3.4. WC evolution

In order to examine the evolution of WC particles during the two AM approaches, SEM micrographs with higher magnification of the CSAM and SLM composites are shown in Fig. 7. As presented in Fig. 7a, WC particles experienced a small plastic deformation and are distributed around the MS300 particles. As shown in Fig. 7a, the deposited WC particles would be broken or even be detached from the deposited composite upon the impact of subsequent WC particles.

As for the SLM composite, due to the heat radiations from the laser source at the top of the molten pool, all MS300 particles were completely melted and only partial WC particles can be observed. As shown in Fig. 7b, the WC particles are present in a variety of molten states at the different locations of the molten pool. However, there exists slight WC spots with a relative sizable concentration gradient area in the middle of the molten pool. The WC particles cannot be completely melted due to the heat conduction under the laser beam. Meanwhile, the grain size of the MS300 matrix is found to increase from the bottom to the top, which also corresponds well with the temperature distribution along the vertical direction. Thus, it can be concluded that such evolution of WC particles under the effect of the high thermal energy input by the laser beam, directly leads to the relatively high microhardness of the

SLM composite. Besides, layer-by-layer building under the interaction of laser beam can always heat treat previously built material,which can also indirectly contribute to the microhardness value.

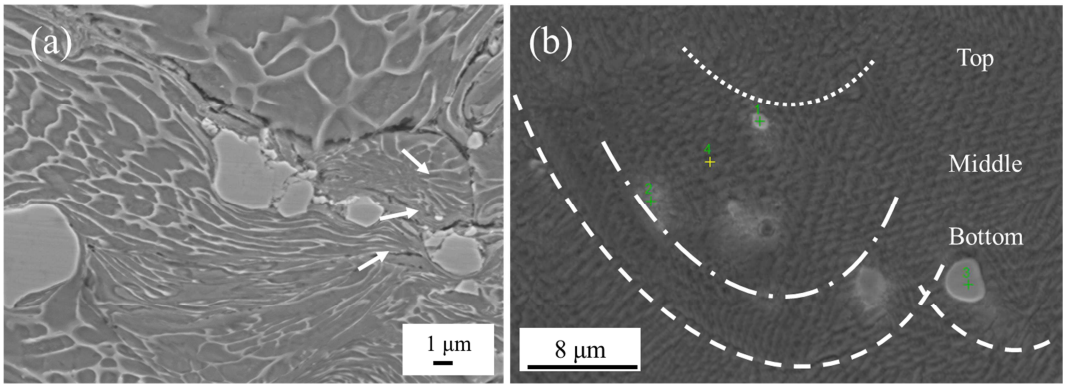

Fig. 7 SEM micrographs of CSAM (a) and SLM (b) processed composites.

To further specify the chemical composition of the WC phase distributed in the composites by CSAM and SLM, EDS line scan was carried out and the results are shown in Fig. 8. As for CSAM composites (see Fig. 8a), it can be seen that an intimate contact is formed between the two phases of MS300 and WC. The EDS line scan was conducted across the WC particles and the interface, and the results are given in Fig. 8b. The main elements of the matrix (i.e., Fe and Ni) and the abundant elements of the particles (W and C), were selected. The concentration of elements changes sharply which demonstates that there is no obvious diffusion between them.

As shown in Fig. 8c, unclear contours can be observed around the partially melted WC phase in SLM composites. In order to evaluate the distribution of elements, EDS line scan was conducted across the WC particle and the affected region. As shown in Fig. 8d, the concentration of W element gradually increases at the interface while the ones of Fe and Ni decrease gradually. The fluctuation of the C element is not apparent because of its relatively low atomic mass. The EDS line scan result indicates that the high thermal energy input by laser beam, provided the necessary activation energy for diffusion. Besides, W and C atoms from WC particles diffused mutually with Fe and Ni atoms released from the matrix. During the mutual diffusion, the chemical diffusion process ended in the formation of carbides of different atomic ratios [45]. Therefore, the concentration gradient interface can only appear within a certain distance from a WC particle surface.

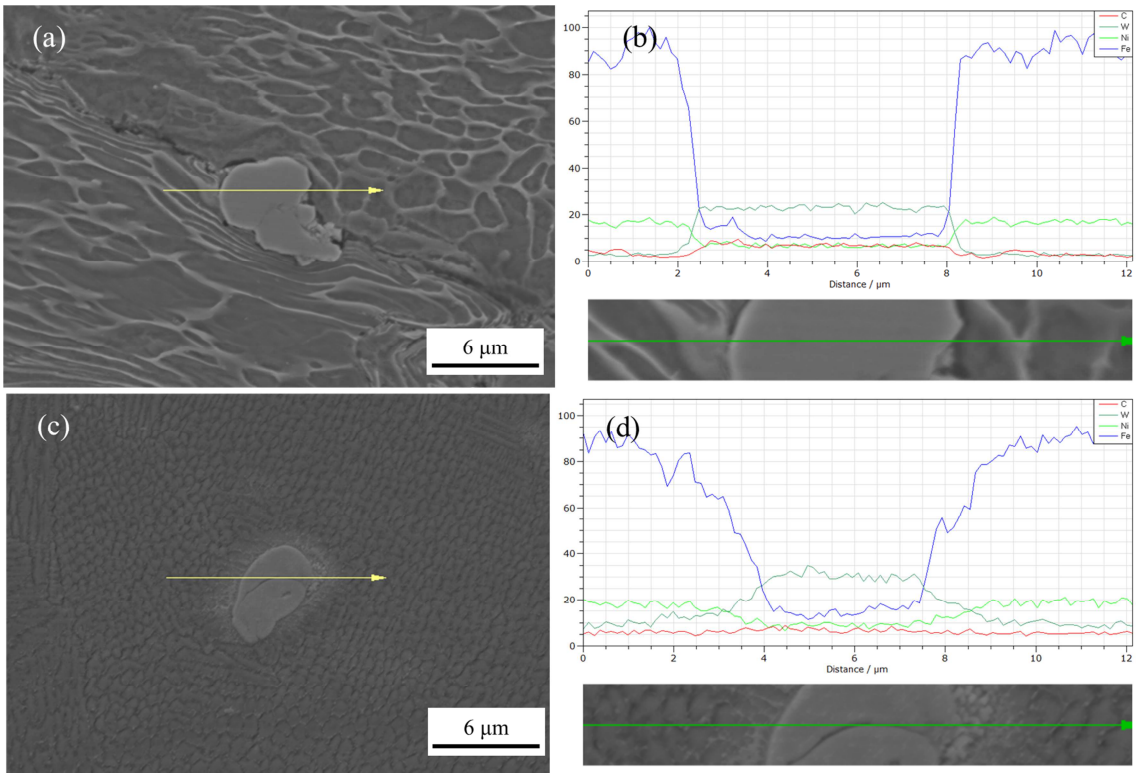

Fig. 8 Linear EDS elements analysis of the WC phase in CSAM (a and b) and SLM (c and d) composites.

In order to observe the chemical diffusion in SLM composite, a high magnification STEM observation of the bonded WC particle is shown in Fig. 9 (a). WC particles were effectively embeded and bonded tightly with the MS300 matrix without gaps at the interface. Besides, a dendritic microstructure was noticed near the surrending material and its orintentation was radially outward around the interface of WC particle. The formation of dendritic microstructure is mianly due to the diffusion and in-situ reactions between coressponding elemets. EDS examination analysis for different elements are displayed in Fig. 9 (b-f). To a certain extent, W atoms from the WC particle was dissolved into the MS300 matrix, while few Fe and Ni atoms from the matrix were diffused into the reinforcement particle. This can be explained by elements concentration gradient during the laser processing. On one hand, when the W atoms desolventize from the partially molten, WC particles incline to diffuse into the dislocation lines and vacancies of the molten MS300 matrix, as a result of reduced lattice distortion of the matrix and free energy of the system [45]. On the other hand, few Fe and Ni atoms can pass throuth the diffusion layer to reach the dense reinforcement particles due to the rapid densification rate. One should notice that this laser processes are limited in treated volume and treatment time, so that diffusion processes may not take place as expected from typical melt-metallurgy

processes. So it is reasonable to find more W and C (see Fig. 9 (d)) in the graded interfacial layer, while Fe and Ni are less (see Fig. 9 (c and d)).

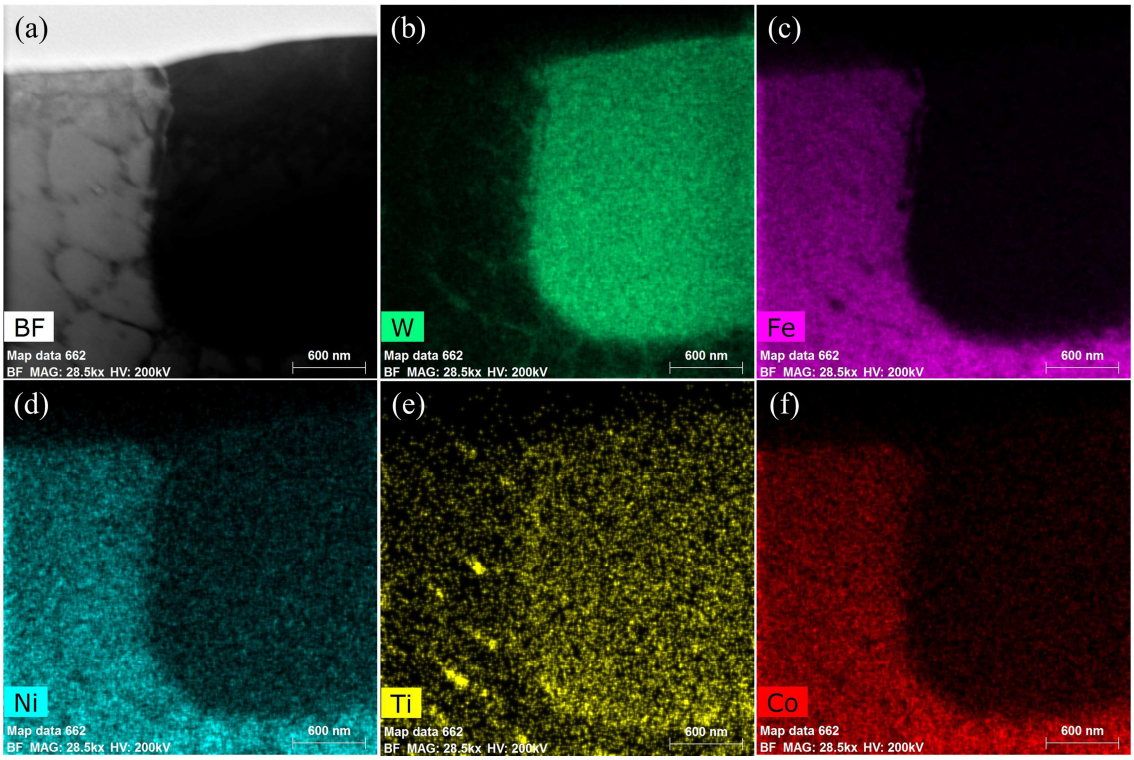

Fig. 9 (a) STEM image of the WC particle embedded into the MS300 matrix; (b-f) maping EDS elements analysis of the interface: (b) W, (c) Fe, (d) Ni, (e) Co, (f) Ti.

3.5. Tribological behaviours

3.5.1. Coefficient of friction (COFs) and wear rates

Fig. 10 shows two curves depicting the evolution of the coefficient of friction (COF) for the composites fabricated by the two different AM methods. The SLM composite shows a higher average COF (value of 0.52) than that of CSAM composite (0.49). It can be clearly seen that the COF of the CSAM composite experiences a rapid increase at the beginning and a folllowing slow decrease before 2000 laps corresponding to 37.68m, and then it stabilizes at a certain level. On the contrary, the COF of the SLM composite presents a relatively stable evolution. The wear rates and the cross-sections of the wear tracks of the CSAM and SLM composites are shown in Fig. 11. Apparently, the wear rate of the CSAM composite with 4.96×10^{-5} $mm^3N^{-1}m^{-1}$ is about 10 times higher than that of SLM composite (4.6×10^{-6} $mm^3N^{-1}m^{-1}$).

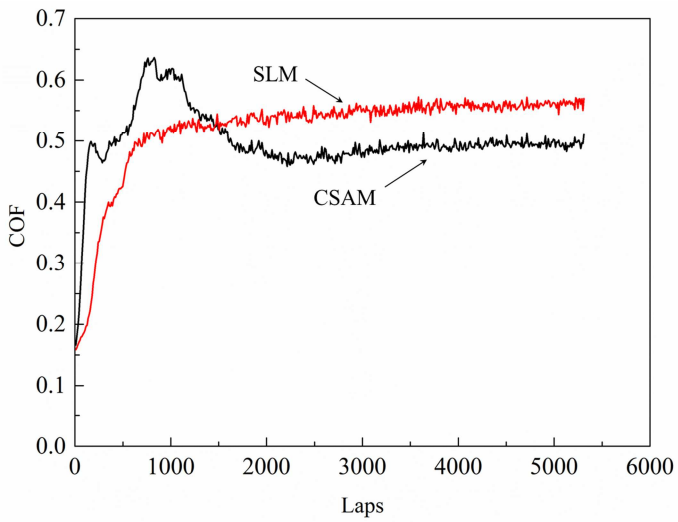

Fig. 10 Evolution curves of the COF for the CSAM and SLM-processed WC/MS300 composites.

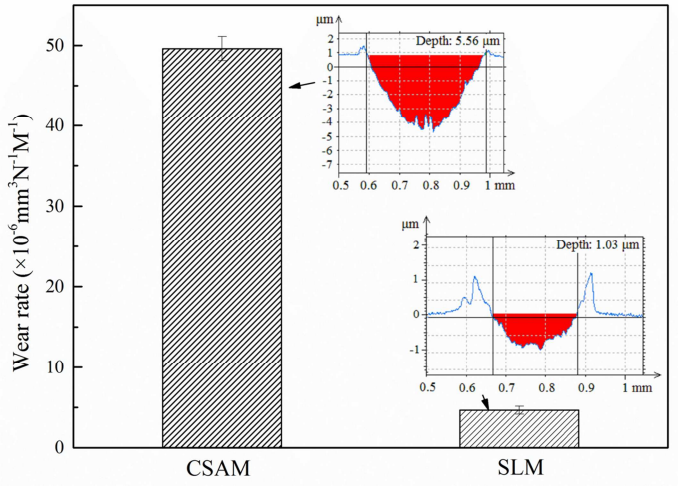

Fig. 11 Comparison of the wear rates and wear cross-sections of the CSAM and SLM-processed composites.

For a better understanding of the changes of the COF, a comprehensive relationship between the wear resistance and the content of the reinforcement WC particle was investigated. At first, the different ~~contents and~~ distributions of the WC phase, have a significant effect on the friction coefficient. According to the cross-sectional morphology in Fig. 4, the distribution of the WC phase in the CSAM and SLM composites, shows a significant influence on the COF and the wear behavior. The calculated relative contents of WC phase in the CSAM and SLM composites are 3.9 and 0.6 respectively. As for the CSAM composite with a relatively high WC content and low densification rate, the aggregation of reinforcement WC particles with high size leads to fluctuations of the COF during the initial stage of wear tests. As the process of dry sliding test, the formation of a surface oxidation

layer promotes the transformation of the oxidation wear process, which leads to a lower COF wear after 2000 laps. The details of the wear process transformation are given in the following parts.

The average COF value of the SLM composite with lower WC content is 0.52, which is higher than that of the CSAM composite (0.50). As mentioned in the formation mechanism of the SLM composite, the high thermal energy input by the laser beam promotes the melting and diffusion of WC particles in the matrix, which also leads to the strong bonding between these two phases. Thereby, even though the SLM composite possesses a higher average COF value, its wear rate is much lower than that of the CSAM composite, due to the strong cohesion between the particles which can be illustrated in Fig. 9. Thus, it is reasonable to believe that in the SLMed WC/MS300 part, the bonding strength of WC particles with the matrix is much higher due to grain boundaries diffusion reactions. In this study, the CSAM sample comprise obviously inner particle boundaries, which can be the weak point in the wear load. This component with the inherent defects or cracks possess dissimilar mechanical properties with the the SLM ones which is fabricated through full metallurgical bonding.

3.5.2. Worn surface morphology and mechanism

To investigate the wear mechanisms, SEM images of the worn surfaces are displayed in Fig. 12 for the two composites. As shown in Fig. 12a, oxide layers are found on the worn surface of the CSAM composite. According to the worn morphology in the high magnification SEM micrograph given in Fig. 12c, some WC particles can be found aggregating on the worn surface. The contact between the sliding counterpart and the matrix with relatively low hardness promotes the exposure of the reinforcement WC particles from the composite. Such direct contact between the WC particles and the counterpart leads to the looseness of WC particles. Due to the mechanical interlocking of WC particles in the matrix, the detachment of WC particles from the matrix can be seen under the low bonding strength.

The EDS results from the inset of Fig. 13b demonstrate that the composition of this layer is mainly iron oxides. Therefore, the oxides would be more easily abraded by the counterpart and well-bonded WC particles during the adhesion wear process. Then, the surface oxidation layers would be crushed into the wear interface under the shearing friction force. This shows a typical feature of the oxidation wear process. However, the iron oxide particles distribution on the worn tracks contributes to a third-body abrasion in the sliding process and gives rise to heterogeneous deformations, which could

significantly decrease the coefficient of friction and prevent serious ploughing of the worn tracks. Consequently, adhesion between the sliding pairs is no longer a major factor of the tribological behavior. Meanwhile, it should be noted that the original oxide film on the feedstock particle will be crushed into fragments during the high-velocity impact in cold spray. The traditional theory on the oxide-film cleaning effect [46] states that the broken oxides will be pushed to the rim of deformed particles by the extrusion of metal jet as a result of adiabatic shear instability [17]. It provides a fresh metal surface that is oxide-free enabling the formation of metallurgical bonding. Thus, the detected oxide on worn surface can be ruled out from the original feedstock particle.

As for the CSAM composite, almost no bumps and grooves can be found on the wear tracks (Fig. 12a and c). By comparing with the worn morphology of CSAM composite in Fig. 12a, a smoothing and densifying tribolayer accompanying clearer friction marks, can be found for the SLM composite in Fig. 12b, which means that less deformation happened during the same sliding procedure. Neither significant cracking nor fracturing is observed in the SLM composite, and some WC particles are found on the worn surface. As shown in Fig. 12d, embedded WC particles remain on the wear surface of the SLM composite. After experiencing a huge shear stress, no delamination happened to the WC particles. In other words, the particle alloyed in the SLM-processed composite is stronger than the mechanical interlocking in the CSAM composite, which can also be proved by the difference in the densification rates (Fig. 5). As a result, the wear rate of the SLM composite was much lower compared with that of the CSAM composite, as can be seen in Fig. 11. Furthermore, the SLM composite possesses a better wear resistance ability. It is reasonable to consider that the mechanism of material removal during sliding is abrasion. In Fig. 12d, the high magnification SEM image presents WC particles with a semi-polished surface. Almost no obvious scratches can be found, revealing the relatively stable changes of the friction coefficient and wear behavior. Besides, relatively fine debris appeared on the friction path of the WC particles. It is thus reasonable to consider that adhesive wear is the main wear mechanism for the SLM composite.

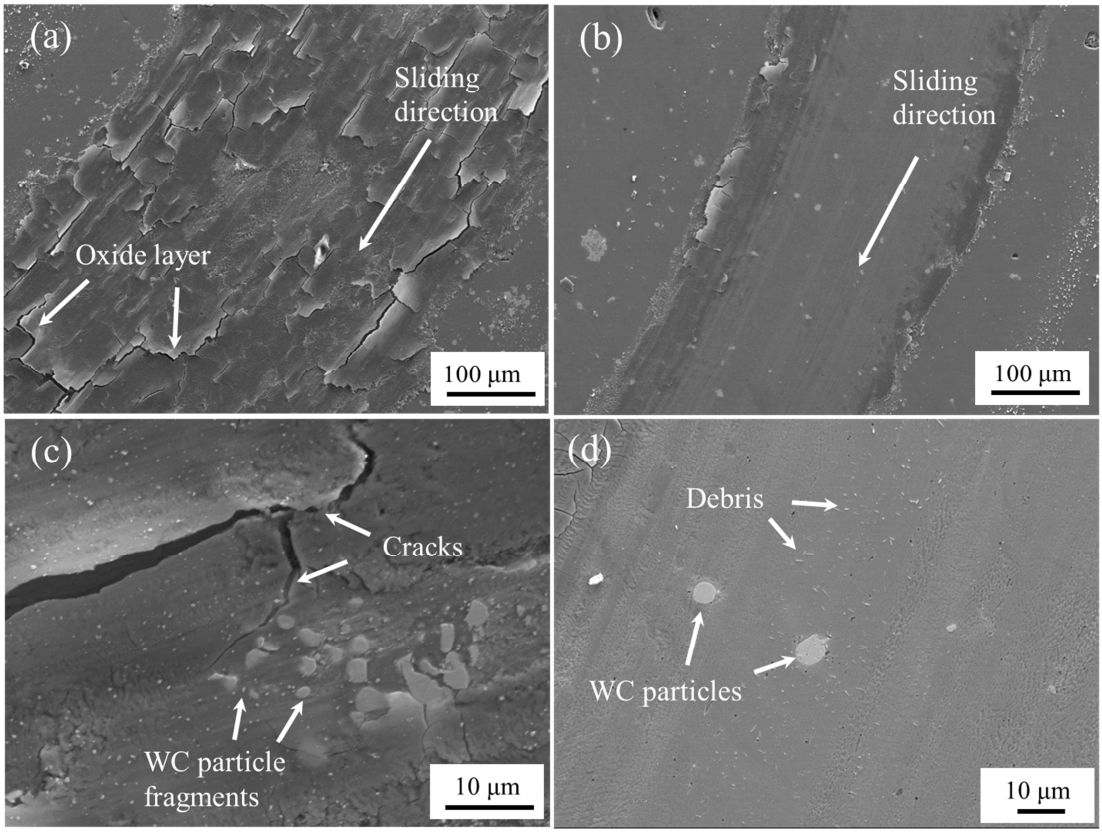

Fig. 12 SEM micrographs of the worn surface morphologies and worn tracks at high magnification, for the CSAM (a and c) and SLM-processed (b and d) parts.

As the EDS result is given in Fig. 13d, elements Fe, Ni and Mo were released from the maraging steel matrix, and C and W from WC particles. Oxygen element was detected on the slightly worn scrap thus attesting that oxidation occured during the heat accumulation from the friction process. Such reaction between the reinforcement particles and the MS300 matrix promotes the formation of a thick carbide layer (W, M)C_X (M= Fe, Ni, Mo) around WC particles. The resulting coherent bonding between WC particles and the matrix efficiently improves the wear resisitance of the SLM composite.

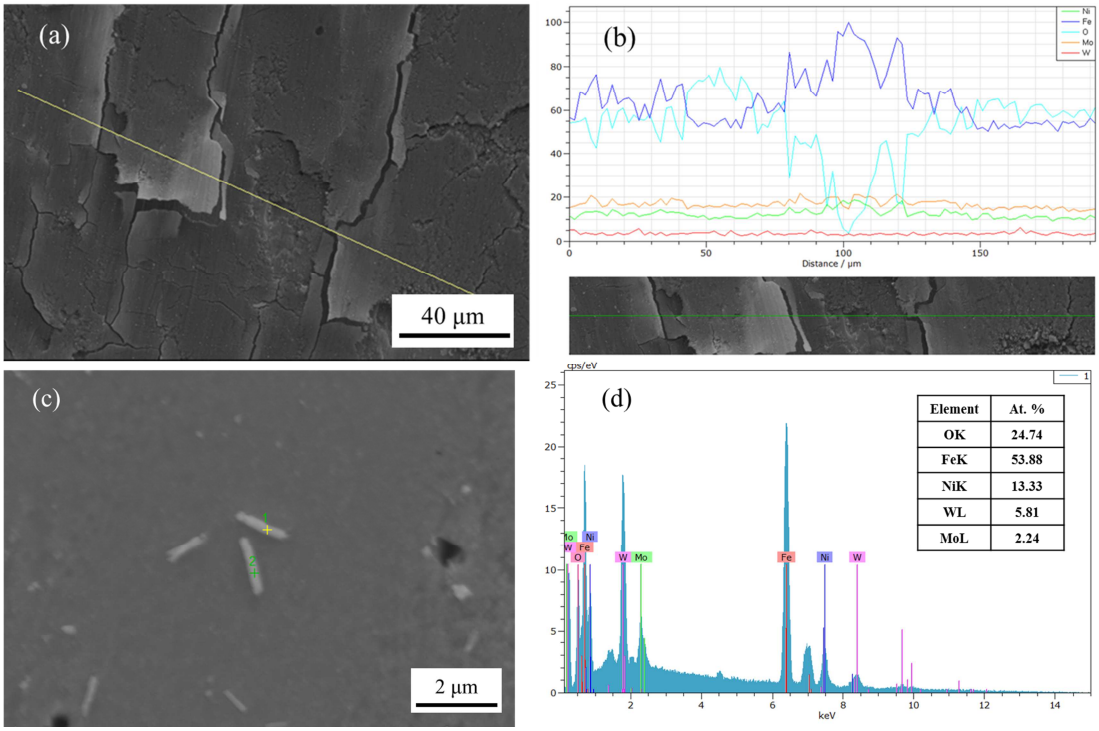

Fig. 13 Linear element analysis of CSAM sample (a) and corresponding EDS element distribution (b); point element analysis of SLM worn debris (c) and corresponding chemical composition (d).

4. Discussion

According to prior work, both the selective laser melting and the cold spraying are considered as effective additive manufacturing methods to fabricate bulk metal matrice composites. According to a recent comparative study by Bagherifard [47], the cold sprayed Inconel 718 samples presented competitive mechanical properties to the SLM samples. However, no profound investigation into the effect of formation mechanism on their microstructure and properties has been addressed in the related work. Thus, in order to better understand the resulting property and microstructure evolution, the formation mechanisms of CSAM and SLM composites are illustrated in Fig. 14a and b respectively.

As etched MS300 particles are shown in Fig. 2, the grain boundaries are homogeneously distributed in the starting particle with a low dislocation density. However, in the CSAM process, such dislocation density of the grain boundary increases with the aggravation of the particle plastic deformation [48, 49]. As microstructure is shown in Fig. 7a, the severe plastic deformation that is indicated by white arrows leads to the formation of elongated dislocation cells and subgrains compared with the grains in feedstock powder (see Fig. 2a). As illustrated in Fig. 14, the particle deformation further breaks the subgrains, and the rotation of broken subgrains completes the recrystallized structure

formation in the shear localization area, which has experienced a severe plastic deformation. Additionaly, the tamping effect by reinforcement particles promotes the plastic deformation of the metal phase. Such evident work hardening effect during the deposition of cold sprayed coating leads to a relatively higher microhardness value (see Fig. 6). Different from MS300 particles, WC particles do not plastically deform during deposition, so that they are surrounded by the subsequent matrix materials. However, the breakup and detachment of embedded WC particles may occur when they are impacted by subsequent WC particles. However, the insufficient plastic deformation of MS300 particle can give rise to the initiation of inter-particle cracks and pores (Fig. 4).

As for the case of SLM (see Fig. 14b), the molten pool was formed under the high energy input by laser beam. With the gradualy movement of laser beam on powder beam, the rapid solidification of the molten pool can help the formation of SLMed sample layer-by-layer. Within the mixed powder, the MS300 particles consisting the matrix of composite experienced complete melting. It can also promote the fully densified microstructure (Fig. 4) and evidently low porosity (Fig. 5) of SLMed composite. With a relatively higher melting point, the WC particle were partial melted so that the residual WC phase can still be found in the microstructure (Fig. 4 and Fig. 7). As shown in Fig. 14b, it is commonly considered that the Marangoni flow is promoted in the molten pool under the effects of both thermal gradient and chemical concentration at the solid/liquid surface. Such Marangoni flow gives rise to the observed WC particle distribution in the MS300 matrix. Meanwhile small WC particles are dissolved at the top of the molten pool with higher temperature, which can be proved by Fig. 8b. On the other hand, comparatively large WC particles with partially melted interface emerged at the bottom of the molten pool due to the weakening flow field. As the EDS line scanning given in Fig. 8, the partially melted WC phases can release W and C atoms and promote the reaction with the metallic matrix. On the contrary, the solid-state consolidation of cold sprayed composite can have significant reinforcing effect by WC particle. Such direct reinforcement can contribute to the significant improvement of the mechanical properties of the composite.

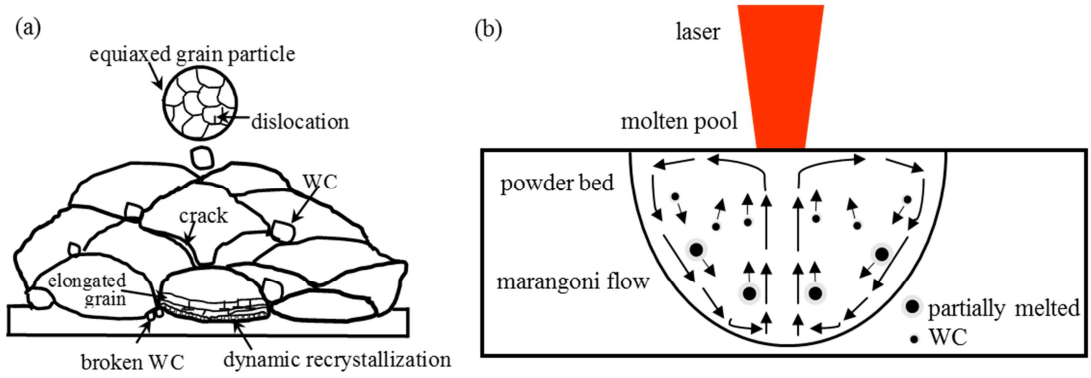

Fig. 14 Illustration of the formation mechanisms of composites manufactured by CSAM (a) and SLM (b).

5. Conclusion

In this study, two different AM technologies of CSAM and SLM were used to fabricate WC particle reinforced maraging steel 300 composites. The microstructures and tribological behaviors of WC/MS300 composites fabricated by the CSAM and SLM processes were investigated. Through the comparison between the different composites, the corresponding characteristics of the different AM technologies are discussed.

1) The WC/MS300 composite manufactured by SLM shows a relatively higher densification and lower porosity than that of the CSAM composite, which revealed different composite formation mechanisms for the different AM methods.
2) According to the microhardness measurements, the CSAM composite possesses a hardness value of 394 $HV_{0.2}$, which is higher than that of the SLM composite (385 $HV_{0.2}$). It can be contributed to the strain or work hardening of the cold sprayed structure. Due to plastic deformations from the successive impact of high-velocity particles and the tamping effect of hard WC particles, the MS300 particles undergoes a severe work-hardening, which leads to the increase of the microhardness of the CSAM composite. Meanwhile the partial melting of WC particles in the SLM composite leads to the enhancement of the microhardness of SLM composite.
3) Different evolution features of WC particles were found for the two composites. In the CSAM one, the reinforcement WC particles experienced little plastic deformation and are distributed around MS300 particles. Mechanical interlocking is the main bonding mechanism of WC particles in the CSAM composite. As for the SLM composite, completely or partially melted WC particles are

uniformly distributed and firmly welded with the metal matrix, due to the molten metal flow caused by the high energy input of the laser beam.

4) The CSAM processed composite is featured by plastically deformed metal particles with almost intact WC particles embeded at the interfaces between MS300 particles, which is owing to the low temperature feature of the CS technology. However, the microstructure of the SLM processed composite revealed dendritic solidification patterns distributed perpendicular to the powder bed plane.

5) Different tribological behavior were presented for the different composites owing to the distinct morphologies. The relatively high WC content and low densification rate leads to the aggregation of the reinforcement WC particles in the CSAM composite and further fluctuations of the COF during the initial stage of the wear tests. The subsequent formation of a surface oxidation layer promotes the transformation of the oxidation wear process, which leads to an excellent wear performance after 2000 laps. Meanwhile, the main wear mechanism of the SLM composite is abrasion. Almost no obvious scratches can be found on the worn morphology of the SLM composite, revealing the stable evolution of the friction coefficient and wear behavior.

Acknowledgements

As one of the authors, X.C YAN, is grateful for the financial supports provided by the China Scholarship Council (NO. 201504490031), Guangdong Provincial Science and Technology Department, International Cooperation Base Construction Project China-France Modern Material Surface Engineering Technology International Cooperation Base Construction (NO, 2014B050502008), Guangzhou Science and Technology Innovation Committee, Production and Research Collaborative Innovation Major Projects of Foreign Cooperation Projects, Research and Application of Laser 3D Printing Die-Casting Mold Technology (NO, 2016201604030028), Guangdong Provincial Science and Technology Department, Provincial Scientific Research Institutions Reform and Innovation Projects, Laser 3D Printing Technology and Application of Innovative Research Team Building (NO, 2016B070701020), Zhongshan Science and Technology Bureau, Zhongshan City-Guangdong Province Science Institute of Technical Transfer Special Funds Project, Study on Industrial Application of Laser 3D Printing Type Cooling Injection Mold (NO, 2016G1FC0004), Guangdong Provincial Science and Technology Department, Research Platform

Environment and Capacity Building Special Fund Project, China-UK Joint Manufacturing Technology Research Center-3D Printing Technology Innovation Platform (NO, 2016GDASPT-03102), Guangdong Provincial Science and Technology Department Research Platform Environment and Capacity Building Projects of Special Funds, "Modern Materials Surface Engineering Technology National Engineering Laboratory" Scientific Research Platform to Enhance Capacity (NO, 2016GDSPT-0206).

References

[1] D. Gu, W. Meiners, K. Wissenbach, R. Poprawe, Laser additive manufacturing of metallic components: materials, processes and mechanisms, Int Mater Rev 57(3) (2012) 133-164.

[2] H. Lipson, M. Kurman, Fabricated: The new world of 3D printing, John Wiley & Sons2013.

[3] C. Cheah, C. Chua, C. Lee, C. Feng, K. Totong, Rapid prototyping and tooling techniques: a review of applications for rapid investment casting, Int J Adv Manuf Technol 25(3-4) (2005) 308-320.

[4] D.T. Pham, R.S. Gault, A comparison of rapid prototyping technologies, Int J Mach Tool Manu 38(10) (1998) 1257-1287.

[5] M. Markl, C. Körner, Multiscale Modeling of Powder Bed-Based Additive Manufacturing, Ann Rev Mater Res 46(1) (2016) 93-123.

[6] J. Pattison, S. Celotto, R. Morgan, M. Bray, W. O'Neill, Cold gas dynamic manufacturing: A non-thermal approach to freeform fabrication, Int J Mach Tool Manu 47(3–4) (2007) 627-634.

[7] A. Sova, S. Grigoriev, A. Okunkova, I. Smurov, Potential of cold gas dynamic spray as additive manufacturing technology, Int J Adv Manuf Tech 69(9-12) (2013) 2269-2278.

[8] P. Mercelis, J.-P. Kruth, Residual stresses in selective laser sintering and selective laser melting, RAPID PROTOTYPING J 12(5) (2006) 254-265.

[9] S.A. Khairallah, A.T. Anderson, A. Rubenchik, W.E. King, Laser powder-bed fusion additive manufacturing: Physics of complex melt flow and formation mechanisms of pores, spatter, and denudation zones, Acta Mater 108 (2016) 36-45.

[10] A. Simchi, F. Petzoldt, H. Pohl, On the development of direct metal laser sintering for rapid tooling, J Mater Process Technol 141(3) (2003) 319-328.

[11] R. Morgan, C. Sutcliffe, W. O'neill, Density analysis of direct metal laser re-melted 316L stainless steel cubic primitives, J Mater Sci 39(4) (2004) 1195-1205.

[12] H. Assadi, F. Gartner, T. Stoltenhoff, H. Kreye, Bonding mechanism in cold gas spraying, Acta Mater 51(15) (2003) 4379-4394.

[13] S. Yin, X. Wang, X. Suo, H. Liao, Z. Guo, W. Li, C. Coddet, Deposition behavior of thermally softened copper particles in cold spraying, Acta Mater 61(14) (2013) 5105-5118.

[14] M. Grujicic, J. Saylor, D. Beasley, W. DeRosset, D. Helfritch, Computational analysis of the interfacial bonding between feed-powder particles and the substrate in the cold-gas dynamic-spray process, Appl Surf Sci 219(3) (2003) 211-227.

[15] C. Chen, Y. Xie, S. Yin, M.-P. Planche, S. Deng, R. Lupoi, H. Liao, Evaluation of the interfacial bonding between particles and substrate in angular cold spray, Mater Lett 173 (2016) 76-79.

[16] C. Huang, W. Li, Y. Feng, Y. Xie, M.-P. Planche, H. Liao, G. Montavon, Microstructural evolution and mechanical properties enhancement of a cold-sprayed Cu Zn alloy coating with friction stir processing, Mater Charact 125 (2017) 76-82.

[17] H. Assadi, H. Kreye, F. Gärtner, T. Klassen, Cold spraying – A materials perspective, Acta Mater 116 (2016) 382-407.

[18] W. Li, K. Yang, S. Yin, X. Yang, Y. Xu, R. Lupoi, Solid-state additive manufacturing and repairing by cold spraying: A review, J. Mater. Sci. Technol. (2017).

[19] L. Ajdelsztajn, J.M. Schoenung, B. Jodoin, G.E. Kim, Cold spray deposition of nanocrystalline aluminum alloys, Metallurgical and Materials Transactions A 36(3) (2005) 657-666.

[20] P. Richer, B. Jodoin, L. Ajdelsztajn, Substrate roughness and thickness effects on cold spray nanocrystalline Al− Mg coatings, J Therm Spray Technol 15(2) (2006) 246-254.

[21] C. Chen, S. Gojon, Y. Xie, S. Yin, C. Verdy, Z. Ren, H. Liao, S. Deng, A novel spiral trajectory for damage component recovery with cold spray, Surf Coat Technol 309 (2017) 719-728.

[22] W.Y. Li, R.R. Jiang, C.J. Huang, Z.H. Zhang, Y. Feng, Effect of cold sprayed Al coating on mechanical property and corrosion behavior of friction stir welded AA2024-T351 joint, Mater Des 65 (2015) 757-761.

[23] C.-J. Li, W.-Y. Li, Deposition characteristics of titanium coating in cold spraying, Surf Coat Technol 167(2–3) (2003) 278-283.

[24] G. Bae, S. Kumar, S. Yoon, K. Kang, H. Na, H.-J. Kim, C. Lee, Bonding features and associated mechanisms in kinetic sprayed titanium coatings, Acta Mater 57(19) (2009) 5654-5666.

[25] X.-T. Luo, Y.-K. Wei, Y. Wang, C.-J. Li, Microstructure and mechanical property of Ti and Ti6Al4V prepared by an in-situ shot peening assisted cold spraying, Mater Des 85 (2015) 527-533.
[26] P. Dupuis, Y. Cormier, M. Fenech, B. Jodoin, Heat transfer and flow structure characterization for pin fins produced by cold spray additive manufacturing, Int J Heat Mass Tran 98 (2016) 650-661.
[27] V.K. Champagne, The repair of magnesium rotorcraft components by cold spray, Journal of Failure Analysis and Prevention 8(2) (2008) 164-175.
[28] D.D. Gu, W. Meiners, K. Wissenbach, R. Poprawe, Laser additive manufacturing of metallic components: materials, processes and mechanisms, Int Mater Rev 57(3) (2012) 133-164.
[29] B. AlMangour, D. Grzesiak, J.-M. Yang, In situ formation of TiC-particle-reinforced stainless steel matrix nanocomposites during ball milling: Feedstock powder preparation for selective laser melting at various energy densities, Powder Technology 326 (2018) 467-478.
[30] B. AlMangour, D. Grzesiak, J.-M. Yang, In-situ formation of novel TiC-particle-reinforced 316L stainless steel bulk-form composites by selective laser melting, Journal of Alloys and Compounds 706 (2017) 409-418.
[31] F. Chang, D. Gu, D. Dai, P. Yuan, Selective laser melting of in-situ Al4SiC4+SiC hybrid reinforced Al matrix composites: Influence of starting SiC particle size, Surface and Coatings Technology 272 (2015) 15-24.
[32] S. Dadbakhsh, L. Hao, Effect of Al alloys on selective laser melting behaviour and microstructure of in situ formed particle reinforced composites, J Alloy Compd 541 (2012) 328-334.
[33] J. Jue, D. Gu, K. Chang, D. Dai, Microstructure evolution and mechanical properties of Al-Al2O3 composites fabricated by selective laser melting, Powder Technology 310 (2017) 80-91.
[34] B. He, K. Chang, W. Wu, C. Zhang, The formation mechanism of TiC reinforcement and improved tensile strength in additive manufactured Ti matrix nanocomposite, Vacuum 143 (2017) 23-27.
[35] M. Xia, A. Liu, Z. Hou, N. Li, Z. Chen, H. Ding, Microstructure growth behavior and its evolution mechanism during laser additive manufacture of in-situ reinforced (TiB+TiC)/Ti composite, Journal of Alloys and Compounds 728 (2017) 436-444.
[36] J.J. Yang, J. Han, H.C. Yu, J. Yin, M. Gao, Z.M. Wang, X.Y. Zeng, Role of molten pool mode on formability, microstructure and mechanical properties of selective laser melted Ti-6A1-4V alloy, Mater Des 110 (2016) 558-570.

[37] H. Attar, M. Bönisch, M. Calin, L.-C. Zhang, S. Scudino, J. Eckert, Selective laser melting of in situ titanium–titanium boride composites: Processing, microstructure and mechanical properties, Acta Mater 76 (2014) 13-22.

[38] L.F. Vanswam, R.M. Pelloux, N.J. Grant, Fatigue Behavior of Maraging-steel 300, Metall Trans 6(1) (1975) 45-54.

[39] K. Kempen, E. Yasa, L. Thijs, J.P. Kruth, J. Van Humbeeck, Microstructure and mechanical properties of Selective Laser Melted 18Ni-300 steel, Phys Procedia 12, Part A (2011) 255-263.

[40] T. Hermann Becker, T. Hermann Becker, D. Dimitrov, D. Dimitrov, The achievable mechanical properties of SLM produced Maraging Steel 300 components, RAPID PROTOTYPING J 22(3) (2016) 487-494.

[41] M. Yu, X.K. Suo, W.Y. Li, Y.Y. Wang, H.L. Liao, Microstructure, mechanical property and wear performance of cold sprayed Al5056/SiCp composite coatings: Effect of reinforcement content, Appl Surf Sci 289 (2014) 188-196.

[42] T. DebRoy, H.L. Wei, J.S. Zuback, T. Mukherjee, J.W. Elmer, J.O. Milewski, A.M. Beese, A. Wilson-Heid, A. De, W. Zhang, Additive manufacturing of metallic components – Process, structure and properties, Prog Mater Sci 92(Supplement C) (2018) 112-224.

[43] Y.Q. Ren, P.C. King, Y.S. Yang, T.Q. Xiao, C. Chu, S. Gulizia, A.B. Murphy, Characterization of heat treatment-induced pore structure changes in cold-sprayed titanium, Mater Charact 132(Supplement C) (2017) 69-75.

[44] V.K. Champagne, D.J. Helfritch, M.D. Trexler, B.M. Gabriel, The effect of cold spray impact velocity on deposit hardness, Model Simul Mater Sc 18(6) (2010) 8.

[45] T. Rong, D. Gu, Q. Shi, S. Cao, M. Xia, Effects of tailored gradient interface on wear properties of WC/Inconel 718 composites using selective laser melting, Surf Coat Technol 307, Part A (2016) 418-427.

[46] C. Chen, Y. Xie, R. Huang, S. Deng, Z. Ren, H. Liao, On the role of oxide film's cleaning effect into the metallurgical bonding during cold spray, Mater Lett 210(1) (2018) 199-202.

[47] S. Bagherifard, G. Roscioli, M.V. Zuccoli, M. Hadi, G. D'Elia, A.G. Demir, B. Previtali, J. Kondás, M. Guagliano, Cold Spray Deposition of Freestanding Inconel Samples and Comparative Analysis with Selective Laser Melting, J Therm Spray Technol (2017) 1-10.

[48] C. Huang, W. Li, Y. Feng, Y. Xie, M.-P. Planche, H. Liao, G. Montavon, Microstructural evolution and mechanical properties enhancement of a cold-sprayed CuZn alloy coating with friction stir processing, Mater Charact 125 (2017) 76-82.

[49] Y. Zou, W. Qin, E. Irissou, J.-G. Legoux, S. Yue, J.A. Szpunar, Dynamic recrystallization in the particle/particle interfacial region of cold-sprayed nickel coating: Electron backscatter diffraction characterization, Scr. Mater. 61(9) (2009) 899-902.